Dear Editor,

Thank you for handling our manuscript and providing us with these additional referee's comments. A point by point response to these comments is provided below. The manuscript and the supplementary material with the changes marked-up are also in this document after the referee response.

Best regards,

Patricia Zunino, Herlé Mercier and Virginie Thierry

The authors have tried to address the main comments on their method, previously using a density criterion only to determine a mixed layer and now considering temperature and salinity as well. Their current criterion is still rather wide. The authors state that "The temperature threshold of 0.1°C and the salinity threshold of 0.012 were selected because they correspond to a threshold of 0.01 kg m-3 in density that was previously shown to perform well in the subpolar gyre (Piron et al., 2016)". This is only true if either salinity or temperature is at this threshold, if both are the density difference can be as big as 0.2 kg/m^3.

In her first review of our manuscript, the reviewer noted that our determination of the MLD based only on a density criteria failed when density compensated temperature and salinity anomalies occurred in the mixed layer. The criteria in temperature and salinity that we added in our revision were chosen to address this problem. When temperature and salinity anomalies are density compensated, they do not add together and selecting a criteria for determining the MLD from the temperature or salinity profiles with a threshold equivalent to the one used for density seems correct to us. Visual inspection confirms this. Of course, if temperature and salinity profiles are nearly homogeneous or not compensated in density, the criteria in density sets the MLD, but these were not cases that the reviewer identified as problematic. We added the following sentence in the revised manuscript: "The criteria on temperature and salinity were chosen to perform well when temperature and salinity anomalies within the density-defined mixed layer are density compensated."

The authors attempt to compare their method with earlier publications, however the comparison is made incorrectly stating "Following de Jong et al. method's, three MLD were defined as the depths were the standard deviations were smaller than 0.05 kg m-3 , 0.05°C and 0.005 for density, temperature and salinity, respectively", the error being that the standard deviations were not used as a threshold to determine the bottom of the MLD but as a final check leading to discarding misidentified MLDs (as described in the paper). Since this comparison now features in the supplementary materials it will need to be corrected.

The present manuscript mostly compares the identified MLDs to those we identified in the winter of 2014-2015 (de Jong et al., 2018). For those MLD we used a criteria of "0.015°C for temperature, 0.005 for salinity, and 0.0025 kg m–3 for potential density". "The resulting MLDs of all three variables had to be within 50 dbar to be accepted, after which the temperature-derived MLDs were chosen as final MLDs." Running this criteria on the specific float profiles shown in Figure 2 of the manuscript results in the deepest MLD (of 570 dbar) observed in the profile of float 5904772, cycle 33. For the

other profile shown in the Figure 2, and the supplementary material, our methods gives a MLD of only 150 dbar. We made the criteria this strict to sort out actively mixed profiles at the moorings for recently mixed profiles which may have been formed elsewhere and advected to the moorings. Since the authors are looking more of a region than at one specific spot they could make an argument that they can use a wider criterion. In that case I ask that that at least the SI is corrected to show our methods accurately and the difference with earlier estimates be discussed more clearly in the discussion.

We thank the reviewer for noting that. Because of the very strict criteria she used, her method was only adapted to the diagnostic of active mixed layers and thus was not suited to the diagnostic of the MLD our case. Indeed, Straneo et al. (2002) noted that in the ocean interior where baroclinicity is weak there are dynamical reasons for tracer profiles in the mixed layers to be slightly slanted. This confirms that de Jong et al., (2018) criteria, although well suited for their application, are too restrictive in a more general case. Thus we deleted in the supplementary material the comparison between our estimates of MLD and those obtained using de Jong et al.'s method, which was misleading. We noted this information in the supplementary material and we kept the comparison between our results and those obtained using Pickart et al. (2002) method.

In the second paragraph of the results section there is a discussion on the percentage of floats that had deep MLD. This is not very informative, as 1 float with 1 deep ML in the winter of 2017 would give the same percentage as 1 float recording 20 deep MLs in 2015. The percentage of profiles with deep MLs out of all recorded profiles would give a much better indication of the intensity of convection. Overall, this difference in intensity between the winters is mostly neglected in the text ,focusing only on depth (for example lines 364-366 and in the conclusions line 461-467). This is a missed opportunity since the authors have already investigated the likely cause for this difference in intensity, being weaker surface fluxes in the winters after 2014-2015.

Thank you for noting that. We now emphasize this result in the conclusion: "The deep convection of W2015 was observed over a larger region and during a longer period of time than the deep convection events of winters 2016, 2017 and 2018." Otherwise, the percentage of profiles with deep MLs out of all recorded profiles would not necessarily give a better indication of deep convection intensity because spatial and time samplings are not homogeneous in the studied region. We believe that bias due to sampling is less with statistics based on the number of floats.

Line by line comments

Line 50: the "exceptional" here is disputable because we don't have a long enough record to say whether it is really that unusual and because there is such a distinct difference in intensity over the four winters.

Ok, we removed "exceptional" in line 50 of the abstract.

Line 156: The use of Q and Q3 as acronyms for parameters that are not associated is confusing, especially if they occur in subsequent sentences. Consider using a different acronym for Q3. How useful is the third quartile if there are only three profiles with deep MLDs in a winter?

We used Q3 because it is the usual abbreviation for the third quantile in statistic. As explained at the end of section 3.1, Q3 is equivalent to the aggregate maximum depth of convection defined by Yashayaev and Loder (2016). In the revised version of the manuscript we changed the "Q3" to "the aggregate maximum depth of convection".

We consider that Q3 estimate is appropriate because it depends on the values of all the values of the population and is not just the maximum value. Moreover, it allows direct comparison with the results of Yashayaev and Loder (2016) and Piron et al. (2017) who used this estimator.

Line 199: The Monte Carlo method does not address the bias in a reanalysis product as a whole, as observed by Josey et al.

This is correct.

Line 259: "Despite Bsurf* is mainly explained by Q, the accumulated FWF* amounts to ~10 % of the accumulated Q with opposite sign. The air-sea buoyancy flux is 10% lower on average than the air-sea heat flux." This seems to be saying the same thing twice. Consider rephrasing.

Thank you for noting it, we rephrased it as: "B_{surf}* is 10 % lower on average than Q because of the buoyancy addition by FWF*."

Lines 330-340: The discussion of anomalies here would be more interesting/easier to follow if it was immediately linked to local convection and advection pattern as described in lines 393-397.

We are sorry, but we disagree. We believe that lines 393-397 fit well in the discussion section.

References

Straneo, F., M. Kawase, and R. Pickart: Effects of Wind on Convection in Strongly and Weakly Baroclinic Flows with Application to the Labrador Sea, Journal of Physical Oceanography, V32, *https://doi.org/10.1175/1520-0485-32.9.2603*, 2002.

Why did deep convection persist over four consecutive winters (2015-2018) Southeast of Cape Farewell?

Patricia ZUNINO[1], Herlé MERCIER[2] and Virginie THIERRY[3].

1 Altran Technologies, Technopôle Brest Iroise, Site du Vernis , 300 rue Pierre Rivoalon, 29200 Brest, France

2 CNRS, University of Brest, IRD, Ifremer, Laboratoire d'Océanographie Physique et Spatiale (LOPS), IUEM, ZI de la pointe du diable, CS 10070 - 29280 Plouzané, France

3 Ifremer, University of Brest, CNRS, IRD, Laboratoire d'Océanographie Physique et Spatiale (LOPS), IUEM, ZI de la pointe du diable, CS 10070 - 29280 Plouzané, France

Corresponding author: patricia.zuninorodriguez@altran.com

ABSTRACT

After more than a decade of shallow convection, deep convection returned to the Irminger Sea in 2008 and occurred several times since then to reach exceptional convection depths (>1,500 m) in 2015 and 2016. Additionally, deep mixed layers larger than 1600 m were also reported Southeast of Cape Farewell in 2015. In this context, we used Argo data to show that deep convection occurred Southeast of Cape Farewell (SECF) in 2016 and persisted during two additional years in 2017 and 2018 with maximum convection depth larger than 1,300 m. In this article, we investigate the respective roles of air-sea buoyancy flux and preconditioning of the water column (ocean interior buoyancy content) to explain this ~~exceptional~~ 4-year persistence of deep convection SECF. We analyzed the respective contributions of the heat and freshwater components. Contrary to the very negative air-sea buoyancy flux that was observed during winter 2015, the buoyancy fluxes over the SECF region during winters 2016, 2017 and 2018 were close to the climatological average. We estimated the preconditioning of the water column as the buoyancy that needs to be removed (B) from the end of summer water column to homogenize it down to a given depth. B was lower for winters 2016 – 2018 than for the 2008 – 2015 winter mean, due especially to a vanishing stratification from 600 m down to ~1,300 m. It means that less air-sea buoyancy loss was necessary to reach a given convection depth than in the mean and once convection reached 600 m little additional buoyancy loss was needed to homogenize the water column down to 1,300 m. We showed that the decrease in B was due to the combined effects of the local cooling of the intermediate water (200 – 800 m) and the advection of a negative S anomaly in the 1,200 – 1,400 m layer. This favorable preconditioning permitted the very deep convection observed in 2016 – 2018 despite the atmospheric forcing was close to the climatological average.

1. INTRODUCTION

Deep convection is the result of a process by which surface waters loose buoyancy due to atmospheric forcing and sink into the interior of the ocean. It occurs only where specific conditions are met including large air-sea buoyancy loss and favorable preconditioning (i.e. low stratification of the water column) (Marshall & Schott, 1999). In the Subpolar North Atlantic (SPNA), deep convection takes place in the Labrador Sea, South of Cape Farewell and in the Irminger Sea (Kieke & Yashayaev, 2015; Pickart et al. 2003; Piron et al. 2017). Deep convection connects the upper and lower limbs of the Meridional Overturning Circulation (MOC) and transfers climate change signals from the surface to the ocean interior.

Observing deep convection is difficult because it happens on short time and small spatial scales and during periods of severe weather conditions (Marshall & Schott, 1999). The onset of the Argo program at the beginning of the 2000s has considerably increased the number of available oceanographic data throughout the year. Although the sampling characteristics of Argo are not adequate to observe the small scales associated with the convection process itself, Argo data allow the description of the overall intensity of the event and the characterization of the properties of the water masses formed in the winter mixed layer as well (e.g., Yashayaev and Loder, 2017).

In the Labrador Sea, deep convection occurs every year, yet with different intensity (e.g., Yashayaev and Clarke, 2008; Kieke and Yashayaev, 2015). In the Irminger Sea, Argo and mooring data showed that convection deeper than 700 m happened during winters 2008, 2009, 2012, 2015 and 2016 (Väge et al., 2009; de Jong et al., 2012; Piron et al. 2015; de Jong & de Steur, 2016; Fröb et al., 2016; Piron et al. 2017; de Jong et al., 2018). Moreover, in winter 2015, deep convection was also observed south of Cape Farewell (Piron et al., 2017). Excluding winter 2009 when the deep convection event was made possible thanks to a favorable preconditioning (de Jong et al., 2012), all events coincided with strong atmospheric forcing (air-sea heat loss). Prior to 2008, only few deep convection events were reported because the mechanisms leading to it were not favorable (Centurioni and Gould, 2004) or because the observing system was not adequate (Bacon, 1997; Pickart et al., 2003). Nevertheless, the hydrographic properties from the 1990s suggested that deep convection reached as deep as 1,500 m in the Irminger Sea during winters 1994 and 1995 (Pickart et al., 2003), and as deep as 1,000 m south of Cape Farewell during winter 1997 (Bacon et al., 2003).

The convection depths that were reached in the Irminger Sea and south of Cape Farewell at the end of winter 2015 were the deepest observed in these regions since the beginning of the 21st century (de Jong et al., 2016; Piron et al., 2017, Fröb et al., 2016). In this work, we show that deep convection

also happened in a region between south of Cape Farewell and the Irminger Sea (the pink box in Figure 1) every winter from 2016 to 2018. Hereinafter, we will refer to this region as Southeast Cape Farewell (SECF). We investigated the respective role of atmospheric forcing (air-sea buoyancy flux) and preconditioning (ocean interior buoyancy content) in setting the convection intensity. We also disentangled the relative contribution of salinity and temperature anomalies to the preconditioning. The paper is organized as follow. The data are described in Sect. 2. The methodology is explained in Sect. 3. We expose our results in Sect. 4 and discuss them in Sect. 5. Conclusions are listed in Sect. 6.

2. DATA

We used temperature (T), salinity (S) and pressure (P) data measured by Argo floats north of 55°N in the Atlantic Ocean. These data were collected by the International Argo program (http://www.argo.ucsd.edu/), http://www.jcommops.org/) and downloaded from the Coriolis Data Center (http://www.coriolis.eu.org/). Only data flagged as good (quality Control < 3, Argo Data Management Team, 2017) were considered in our analysis. Potential temperature (θ), density (ρ) and potential density anomaly referenced to the surface and 1000 dbar (σ_0 and σ_1, respectively) were estimated from T, S and P data using TEOS-10 (http://www.teos-10.org/).

Code de champ modifié
Code de champ modifié
Code de champ modifié

We used two different gridded products of ocean T and S: ISAS and EN4. ISAS (Gaillard et al., 2016; Kolodziejczyk et al., 2017) is produced by optimal interpolation of *in situ* data. It provides monthly fields, at 152 depth levels, at 0.5° resolution, from 2002 to 2015. Near real time data are also availaible for 2016 and 2018. EN4 (Good et al., 2013) is an optimal interpolation of *in situ* data; it provides monthly T and S at 1° spatial resolution and at 42 depth levels, for the period 1900 to present.

Net air-sea heat flux (Q , the sum of radiative and turbulent fluxes), evaporation (E), precipitation (P), wind stress (τ_x and τ_y) and sea surface temperature (SST) data were obtained from ERA-Interim reanalysis (Dee et al., 2011). ERA-Interim provides data with a time resolution of 12h and a spatial resolution of 0.75°, respectively. The air-sea freshwater flux (FWF) was estimated as E - P.

We used monthly Absolute Dynamic Topographic (ADT), which was computed from the daily 0.25° - resolution ADT data provided by CMEMS (Copernicus Marine and Environment Monitoring Service, http://www.marine.copernicus.eu).

3. METHODS

3.1 Quantification of the deep convection

We characterized the convection in the SPNA in winters 2015-2018 by estimating the mixed layer depths (MLD) for all Argo profiles collected in the SPNA north of 55°N from 1st January to 30th April of each year (Fig. 1). The MLD was estimated as the shallowest of the three MLD estimates obtained by applying the threshold method (de Boyer Montégut et al., 2004) to θ, S and ρ profiles separately. The threshold method computes the MLD as the depth at which the difference between the surface (30 m) and deeper levels in a given property is equal to a given threshold. In case visual inspection of the winter profiles showed a thin stratified layer at the surface, a slightly deeper level (<150 m) was considered as surface reference level. Following Piron et al. (2017), this threshold was taken equal to 0.01 kg m^{-3} for ρ. For θ and S, we selected thresholds of 0.1°C and 0.012 respectively because they correspond to the threshold of 0.01 kg m^{-3} in ρ. The latter was previously shown to perform well in the subpolar gyre on density profiles (Piron et al., 2016). The criteria on temperature and salinity were chosen to perform well when temperature and salinity anomalies within the density-defined mixed layer are density compensated. Our MLD estimates are comparable to those obtained using MLD determination based on Pickart et al. (2002)'s ~~and de Jong et al. (2012)'s~~ methods (see section S1, Fig. S1 and Fig. S2 in supplementary material).

In this paper, deep convection is characterized by profiles with MLD deeper than 700m (colored points in Fig. 1) because it is the minimum depth that should be reached for renewing Labrador Sea Water (LSW) (Yashayaev et al., 2007; Piron et al. 2016). The winter MLD and the associated θ, S and ρ properties were examined for the Labrador Sea and the SECF region by considering the profiles inside the cyan and pink boxes in Fig. 1, respectively. Those two boxes were defined to include all Argo profiles with MLD deeper than 700 m during 2016 – 2018 and the minimum of the monthly ADT for either the SECF region or the Labrador Sea. No deep MLD was recorded in the northernmost part of the Irminger Sea during this period. We computed the maximum MLD and the MLD third quartile (Q_3) from profiles with MLD greater than 700m in each of the two boxes separately. Q_3 is the MLD value that is exceeded by 25% of the profiles and is equivalent to the aggregate maximum depth of convection defined by Yashayaev and Loder (2016). Hereafter, we refer to Q_3 as the aggregate maximum depth of convection. The properties (ρ, θ and S) of the mixed layers were defined for each winter as the vertical mean from 200 m to the MLD of all profiles with MLD deeper than 700 m. For further use, we define the deep convection period as follows. For a given winter, the deep convection period begins the day when the first profile with a deep (>700m) mixed layer is detected and ends the day of the last detection of a deep mixed layer.

3.2. Time series of atmospheric forcing

The air-sea buoyancy flux (B_{surf}) was calculated as the sum of the contributions of Q and FWF (Gill, 1982; Billheimer & Talley, 2013). It reads:

$$B_{surf} = \frac{\alpha\, g}{\rho_0\, c_p}\, Q - \beta\, g\, SSS\, FWF \qquad \text{Eq. (1)}$$

Where α and β are the coefficients of thermal and saline expansions, respectively, estimated from surface T and S. The gravitational acceleration g is equal to 9.8 m s^{-2}, the reference density of sea water ρ_0 is equal to 1026 kg m^{-3} and heat capacity of sea water C_p is equal to 3990 J kg^{-1} °C^{-1}. SSS is the sea surface salinity. Q and FWF are in W m^{-2} and m s^{-1}, respectively.

For easy comparison with previous results, which only considered the heat component of the buoyancy air-sea flux (e.g. Yashayaev & Loder, 2017; Piron et al. 2017; Rhein et al., 2017), B_{surf}, in m^2 s^{-3}, was converted to W m^{-2} following Eq. (2) and noted B^*_{surf}

$$B^*_{surf} = \frac{\rho_0\, c_p}{g\ \alpha}\, B_{surf} \qquad \text{Eq. (2)}$$

The FWF was also converted to W m^{-2} using:

$$\mathrm{FWF}^* = \mathrm{FWF}\ \beta\ SSS\ \frac{\rho_0\, c_p}{\alpha} \qquad \text{Eq. (3)}$$

We also computed the horizontal Ekman buoyancy flux (BF_{ek}), which can be decomposed into the horizontal Ekman heat flux (HF_{ek}) and salt flux (SF_{ek}). Noting :

$$BF_{ek} = -g\ (U_e \partial_x SSD + V_e \partial_y SSD)\, \frac{C_p}{\alpha . g} \qquad \text{Eq. (4)}$$

$$HF_{ek} = -(U_e \partial_x SST + V_e \partial_y SST)\ \rho_0\ C_p \qquad \text{Eq. (5)}$$

$$SF_{ek} = -(U_e \partial_x SSS + V_e \partial_y SSS)\ \frac{\beta\ \rho_0\ C_p}{\alpha} \qquad \text{Eq. (6)}$$

$BF_{ek} = SF_{ek} - HF_{ek}$. U_e and V_e are the eastward and northward components of the Ekman horizontal transport estimated from the wind stress meridional and zonal components. SSD, SST and SSS are ρ, T and S at the surface of the ocean. BF_{ek}, HF_{ek} and SF_e are in J s^{-1} m^{-2}. Because ERA-Interim does not supply SSD or SSS, they were estimated from EN4 as follows. The monthly T and S data at 5 m depth from EN4 were interpolated on the same time and space grid as the air-sea fluxes from ERA-Interim (12h and 0.75°, respectively). SSD was estimated from those interpolated EN4 data (SST and SSS). Properties at 5 m depth were considered to be representative of the Ekman layer. Data at locations

where ocean bottom was shallower than 1000 m were excluded from the analysis to avoid regions covered by sea-ice.

Following Piron et al. (2016), the time series of atmospheric forcing were estimated for the SECF region and the Labrador Sea as follows. First, the gridded air-sea flux data and the horizontal Ekman fluxes were averaged over the pink (SECF region) and cyan (Labrador Sea) boxes (Fig. 1). Second, we estimated the accumulated fluxes from 1 September to 31 August the year after. Finally, we computed the time series of the anomalies of the accumulated fluxes from 1 September to 31 August with respect to the 1993 – 2016 mean.

Finally, in order to quantify the net intensity of the atmospheric forcing over the winter, we computed estimates of B_{surf}* + BF_{ek} fluxes accumulated from 1 September to 31 March the year after. Following Piron et al. (2017), the associated errors were calculated by a Monte Carlo simulation using 50 random perturbations of Q, FWF and B_{surf}. The error amounted to 0.05, 0.04 and 0.03 J m^{-2} for B_{surf}*, Q and FWF*, respectively. The error of the horizontal Ekman buoyancy transport was also estimated by a Monte Carlo simulation and amounted to 0.04 J m^{-2}.

3.3. Preconditioning of the water column

The preconditioning of the water column was evaluated as the buoyancy that has to be removed *(*$B(zi)$) from the late summer density profile to homogenize it down to a depth *zi*. It reads:

$$B(zi) = \frac{g}{\rho_0}\ \sigma_0(zi)zi\ -\ \frac{g}{\rho_0}\int_{z_i}^{o}\sigma_0\ (z)dz \qquad \text{Eq. (7)}$$

σ_0(z) is the vertical profile of potential density anomaly estimated from the profiles of T and S measured by Argo floats in September in the given region (pink or cyan box in Fig. 1).

Following Schmidt and Send (2007), we split B into a temperature (B_θ) and salinity (B_S) term:

$$B_\theta(zi) = -(\ g\ \alpha\ \theta(zi)\ zi -\ g\ \alpha \int_{zi}^{o}\theta(z)\ dz) \qquad \text{Eq. (8)}$$

$$B_S(zi) = g\ \beta\ S(zi)\ zi\ -\ g\ \beta \int_{zi}^{o} S\ (z)dz \qquad \text{Eq. (9)}$$

In order to compare the preconditioning with the heat to be removed and/or air-sea heat fluxes, B, B_θ and B_S are reported in J m^{-2}. B, B_θ and B_S were estimated for a given year from the mean of all September profiles of B, B_θ and B_S. The associated errors were estimated as std(B)/√n, where n is the number of profiles used to compute the September mean values.

4. RESULTS

4.1. Intensity of deep convection and properties of newly formed LSW

We examine the time-evolution of the winter mixed layer SECF since the exceptional convection event of winter 2015 (W2015 hereinafter) (Table 1 and Figs. 1 - 3). In W2015, we recorded a maximum MLD of 1,710 m south of Cape Farewell (Fig. 1a), in line with Piron et al. (2017). The maximum MLD of 1,575 m observed for W2016 (Fig. 1b) is compatible with the ~~MLD~~ active mixed layer > 1,500 m observed in a mooring array in the central Irminger Sea by de Jong et al. (2018). For W2015 and W2016, the aggregate maximum depth of convection~~Q3~~ was 1,205 m and 1,471 m, respectively (Table 1). In W2017, deep convection was observed from three Argo profiles (Fig. 1c and Fig. 2a-c). The maximum MLD of 1,400 m was observed on 16th March 2017 at 56.65°N – 42.30°W. In W2018, the maximum MLD of 1,300 m was observed on 24 February at 58.12°N, 41.84°W (Fig. 1d, 2d-f). Float 5903102 measured MLD of 1,100 m South of Cape Farewell (Fig. 1d), but the estimated MLDs coincided with the deepest levels of measurement of the float so that these estimates, possibly biased low (see Fig. 2d-f), were discarded from our analysis. These results show that convection deeper than 1,300 m occurred during four consecutive winters SECF.

Although the number of floats showing deep convection in W2017 and W2018 was small (3 and 2 floats), it represented a significant percentage of the floats operating in the SECF box at that time. The percentage of floats showing deep convection in the SECF region was computed for the deep convection periods defined from 15 January 2015 to 21 April 2015, 22 February 2016 to 21 March 2016, 16 March 2017 to 4 April 2017 and 24 February 2018 to 26 March 2018. The longest period of deep convection occurred in W2015, the shortest in 2017. The percentage of floats showing deep convection during the deep convection period are 73%, 50%, 33 % and 50%, for winters 2015, 2016, 2017 and 2018, respectively. The lowest % is found for W2017, but it is still substantial. It might reflect that for this specific year floats showing deep MLD were found in the southwestern corner of the SECF box only, suggesting that convection did not occur over the full box.

The properties (σ_0, S and θ) of the end of winter mixed layer were estimated for the four winters (Table 1 and Fig. 3). We observed that, between W2015 and W2018, the water mass formed by deep convection significantly densified and cooled by 0.019 kg m^{-3} and 0.215°C, respectively (see Table 1 and Fig. 3).

In the Labrador Sea, the aggregate maximum depth of convection ~~Q3~~ increased from 2015 to 2018 (see Table 1). Deep convection observed in the Labrador Sea in W2018 was the most intense since the beginning of the Argo era (see Fig. 2c in Yashayaev & Loder, 2016). From W2015 to W2018, newly

formed LSW cooled, became saltier and densified by 0.134°C, 0.013 and 0.023 kg m^{-3}, respectively (Table 1).

The water mass formed SECF is warmer and saltier than that formed in the Labrador Sea (Fig. 3). The deep convection SECF is always shallower than in the Labrador Sea. This result is discussed later in Sect. 5.

4.2. Analysis of the atmospheric forcing Southeast of Cape Farewell

The seasonal cycles of B_{surf}* and Q are in phase and of the same order of magnitude, while FWF*, which is positive and one order of magnitude lower than Q, does not present a seasonal cycle (Fig. S3). The means (1993 – 2018) of the cumulative sums from 1 September to 31 March of Q, FWF* and B_{surf}* estimated over the SECF box (Fig. 1) are - 2.46 ± 0.43 x 10^9 J m^{-2}, 0.28 ± 0.10 x 10^9 J m^{-2} and - 2.22 ± 0.49 x 10^9 J m^{-2}, respectively. ~~Despite~~ B_{surf}* is ~~mainly explained by~~10% lower on average than Q~~,~~ because of the buoyancy addition by ~~the accumulated~~ FWF* ~~amounts to ~10 % of the accumulated Q with opposite sign~~. ~~The air sea buoyancy flux is 10% lower on average than the air sea heat flux.~~ Considering the Ekman transports, the 1993 – 2018 means of the accumulated BF_{ek}, HF_{ek} and SF_{ek} from 1 September to 31 March amount to 0.37 ± 1.15 x 10^8 J m^{-2}, - 0.35 ± 1.36 x 10^8 J m^{-2}, and 0.02 ± 2.04 x 10^8 x 10^9 J m^{-2}, respectively. The horizontal Ekman heat flux is negative, while the Ekman buoyancy flux is positive. This buoyancy gain indicates a southeastward transport of surface freshwater caused by dominant winds from the southwest. Noteworthy, BF_{ek} is one order of magnitude smaller than the B_{surf}*.

The total atmospheric forcing SECF was quantified as the sum of B_{surf}* and BF_{ek}. The anomalies of accumulated fluxes from 1 September to 31 August the year after, with respect to the mean 1993 – 2016, are displayed in Fig. 4 for the SECF box. The grey line in Fig. 4a is the total atmospheric forcing anomaly (B_{surf}* plus BF_{ek}). We identify years with very negative buoyancy loss in the SECF region, e.g. 1994, 1999, 2008, 2012 and 2015. The very negative anomalies of atmospheric forcing in 1999 and 2015 were caused by the very negative anomalies in both B_{surf}* (Fig. 4a) and BF_{ek} (Fig.4d). This correlation was not observed for all the years presenting a negative anomaly of atmospheric forcing. Noteworthy, during W2016, W2017 and W2018, the anomaly of atmospheric forcing was close to zero.

Contrary to the very negative anomaly in atmospheric fluxes over the SECF region observed for W2015, the atmospheric fluxes were close to the mean during W2016, W2017 and W2018.

4.3. Analysis of the preconditioning of the water column Southeast of Cape Farewell

Our hypothesis is that the exceptional deep convection that happened in W2015 in the SECF region favorably preconditioned the water column for deep convection the following winters. The time-evolutions of θ, S, σ_1 and of $\Delta\sigma_1$=0.01 kg m^{-3} layer thicknesses (Fig. 5) show a marked change in the hydrographic properties of the SECF region at the beginning of 2015 caused by the exceptional deep convection that occurred during W2015 (see Piron et al., 2017). The intermediate waters (500 – 1,000 m) became colder than the years before and, despite a slight decrease in salinity, the cooling caused the density to increase (Fig. 5c). Fig. 5d shows $\Delta\sigma_1$=0.01 kg m^{-3} layer thicknesses larger than 600 m appearing at the end of W2015 for the first time since 2002. In the density range 32.36 – 32.39 kg m^{-3}, these layers remained thicker than ~450 m during W2016 to W2018. This indicates low stratification at intermediate depths and a favorable preconditioning of intermediate waters for deep convection initiated by W2015 deep convection. The denser density of the core of the thick layers in 2017 -2018 compared with 2015 - 2016 agrees with the densification of the mixed layer SECF shown in Table 1 and Fig. 3.

B(zi) is our estimate of the preconditioning of the water column before winter (see Method). Fig. 6a shows that, deeper than 100 m, B for W2016, W2017 and W2018 was smaller than B for W2015 or B for the mean W2008 – W2014. Furthermore, for W2016, W2017 and 2018, B remained nearly constant with depth between 600 and 1,300 m, which means that once the water column has been homogenized down to 600 m, little additional buoyancy loss results in the homogenization of the water column down to 1,300 m. Both conditions (i) less buoyancy to be removed and (ii) absence of gradient in the B profile down to 1,300 m indicate a more favorable preconditioning of the water column for W2016, W2017 and W2018 than during W2008 – W2015.

To understand the relative contributions of θ and S to the preconditioning, we computed the thermal (B_θ) and haline (B_S) components of B ($B = B_\theta + B_S$). In general, B_θ (B_s) increases with depth when θ decreases (S increases) with depth. On the contrary, a negative slope in a B_θ (B_S) profile corresponds to θ increasing (S decreasing) with depth and is indicative of a destabilizing effect. The negative slopes in B_θ and B_s profiles are not observed simultaneously because density profiles are stable.

We describe the relative contributions of B_θ and B_s to B by looking first at the mean 2008 – 2014 profiles (discontinuous blue lines in Fig. 6). B_θ accounts for most of the increase in B from the surface to 800 m and below 1,400 m (see Fig. 6a and Fig. 6b). The negative slope in the B_s profile between 800 – 1,000 m (Fig. 6c) slightly reduces B (Fig. 6a) and is due to the decrease in S associated with the

core of LSW (see Fig. 3 in Piron et al. 2016). In the layer 1,000 – 1,400 m, the increase in B (Fig. 6a) is mainly explained by the increase in B_s (Fig. 6c), which follows the increase in S in the transition from LSW to Iceland Scotland Overflow Water (ISOW). This transition layer will be referred to hereinafter as the deep halocline. The evaluation of the preconditioning of the water column was usually analyzed in terms of heat (e.g., Piron et al. 2015; 2017). The decomposition of B in B_θ and B_S reveals that θ governs B in the layer 0 – 800 m. S tends to reduce the stabilizing effect of θ in the layer 800 – 1,000 m, and reinforces it in the layer 1,000 – 1,400 m by adding up to 1×10^9 J m^2 to B.

In order to further understand why the SEFC region was favorably preconditioned during winters 2016 – 2018, we compare the B_θ and B_S of W2017, which was the most favorably preconditioned winter, with the mean 2008 – 2014 (Fig. 7a). From the surface to 1,600 m, B_θ and B_S were smaller for W2017 than for the mean 2008 – 2014. There are two additional remarkable features. First, in the layer 500 – 1000 m, the large reduction of B_θ compared to the 2008 – 2014 mean, mostly explains the decrease in B in this layer. Second, the more negative value of B_s in the layer 1,100 – 1,300 m, compared to the 2008 – 2014 mean, eroded the B_θ slope, making the B profile more vertical for W2017 than for the mean. The more negative contribution of B_s in the layer 1,100 – 1,300 m comes from the fact that the deep halocline was deeper for W2017 (1,300 m, see orange dashed line in Fig. 7a) than for the mean 2008 – 2014 (1,000 m, see blue dashed line in Fig. 7a). Finally, we note that the profiles of $B(z_i)$, $B_\theta(z_i)$ and $B_s(z_i)$ for W2016 and W2018 are more similar to the profiles of W2017 than to those of W2015 or to the mean 2008 – 2014 (see Fig. 6), which indicates that the water column was also favorably preconditioned for deep convection in W2016 and W2018 for the same reasons as in W2017.

The origin of the changes in B is now discussed from the time evolutions of the monthly anomalies of θ, S and σ_0 at 58°N – 40°W that is at the center of the SECF box (Fig. 8). The time evolutions there are similar to those at any other location inside the SECF box. These anomalies were computed using ISAS (Gaillard et al., 2016) and were referenced to the monthly mean of 2002 – 2016. A positive anomaly of σ_0 appeared in 2014 between the surface and 600 m (Fig. 8a) and reached 1,200m in 2015 and beyond. This positive anomaly of σ_0 correlates with a negative anomaly of θ. The latter, however, reached ~1,400 m depth in 2016 that is deeper than the positive anomaly of σ_0. The negative anomaly of S between 1,000 - 1,500 m that appeared in 2015 and strongly reinforced in 2016 caused the negative anomaly in σ_0 between 1,200 – 1,500 m (the density anomaly caused by the negative anomaly in θ between 1,200 – 1,400 m does not balance the density anomaly caused by the negative anomaly of S).

The θ and S anomalies in the water column during 2016 – 2018 explain the anomalies of B, B_θ and B_s and can be summarized as follows. On the one hand, the properties of the surface waters (down to 500 m) were colder than previous years and, despite they were also fresher, they were denser. The density increase in the surface water reduced the density difference with the deeper-lying waters. The intermediate layer (500 – 1000 m) was also favorably preconditioned due to the observed cooling. Additionally, in the layer 1,100 – 1,300 m, the large negative anomaly of B_s with respect to its mean is explained by the decrease in S in this layer, which caused a decrease in σ_0 and, consequently, reduced the σ_0 difference with the shallower-lying water. The decrease in S also resulted in a deepening of the deep halocline.

4.4. Atmospheric forcing versus preconditioning of the water column

We now use the estimates of the accumulated atmospheric forcing (B_{surf}* + BF_{ek}) from 1 September to 31 March the year after (see Fig. S4) to predict the maximum convection depth for a given winter based on September profiles of B. The predicted convection depth is determined as the depth at which B(zi) (Fig. 6a) equals the accumulated atmospheric forcing. The associated error was estimated by propagating the error in the atmospheric forcing (0.05 x 10^9 J m^{-2}). The accumulated atmospheric forcing amounted to -3.21 x 10^9 ± 0.05 J m^{-2}, -2.21 ± 0.04 x 10^9 J m^{-2}, -2.01 ± 0.05 x 10^9 J m^{-2} and -2.47 ± 0.05 x 10^9 J m^{-2} for W2015, W2016, W2017 and W2018, respectively. We found predicted convection depths of 1,085 ± 20 m, 1,285 ± 20 m, 1,415 ± 20 m and 1,345 ± 20 m for W2015, W2016, W2017 and W2018, respectively. We consider the aggregate maximum depth of convection ~~Q3~~ as the observed estimate of the MLD (Table 1). The predicted MLD agrees with the observed MLD within ± 200 m. The differences could be due to errors in the atmospheric forcing (Josey et al., 2018), lateral advection and/or spatial variation in the convection intensity within the box not captured by the Argo sampling.

The satisfactory predictability of the convection depth with our 1-D model indicates that deep convection occurred locally. In spite the atmospheric forcing was close to mean (1993 – 2016) conditions during W2016, W2017 and W2018, convection depths > 1300 m were reached in the SECF region. This was only possible thanks to the favorable preconditioning.

5. DISCUSSION

Deep convection happens in the Irminger Sea and South of Cape Farewell during specific winters characterized by a strong atmospheric forcing (high buoyancy loss), a favorable preconditioning (low stratification) or both at the same time (Bacon et al., 2003; Pickart et al., 2003). In the Irminger Sea, strong atmospheric forcing explained for instance the very deep convection (reaching depth greater

than 1,500 m) observed in the early 90s (Pickart, et al., 2003) and in W2015 (de Jong et al. 2016; Fröb et al., 2016; Piron et al. 2017). It explained as well the return of deep convection in W2008 (Väge et al., 2009) and in W2012 (Piron et al., 2016). The favorable preconditioning caused by the densification of the mixed layer during W2008 favored a new deep convection event in W2009 despite neutral atmospheric forcing (de Jong et al. 2012). Similarly, the preconditioning observed after W2015 in the SECF region favored deep convection in W2016 (this work). The favorable preconditioning persisted three consecutive winters (2016 – 2018) in the SECF region, which allowed deep convection although atmospheric forcing was close to the climatological values. Why did this favorable preconditioning persist in time?

We previously showed that during 2016 – 2018 two hydrographic anomalies affected different ranges of the water column in SECF box: a cooling intensified in the layer 200 – 800 m and a freshening intensified in 1,000 – 1,500 m layer. Those resulted in a decrease in the vertical density gradient between the intermediate and the deeper layers creating a favorable preconditioning of the water column. Note that the cooling affected the layer from surface to 1,400 m and the freshening affected the layer from near surface to 1,600 m, but the cooling and the freshening were intensified at different depth ranges (Fig. 8).

We see in Fig. 5a a sudden decrease in θ in the intermediate layers in 2015 compared to the previous years. It indicates that the decrease in θ of the intermediate layer likely originated locally during W2015 when extraordinary deep convection happened. A slight freshening of the water column (400- 1,500 m) appeared in 2015, likely caused by the W2015 convection event, then it decreased before a second S anomaly intensified in 2016 between 1,100 and 1,400 m (Fig. 8c). It is unlikely that this second anomaly was exclusively locally formed by deep convection because it intensified during summer 2016. Our hypothesis is that this second S anomaly originated in the Labrador Sea and was further transferred to the SECF region by the cyclonic circulation encompassing the Labrador Sea and Irminger Sea at these depths (Daniault et al., 2016; Ollitrault & Colin de Verdière, 2014; Lavander et al., 2000 ; Straneo et al., 2003). It is corroborated by the 2D evolution of the anomalies in S in the layer 1,200 – 1,400 m (Fig. 9): a negative anomaly in S appeared in the Labrador Sea in February 2015, which was transferred southward and northeastward in February 2016 and intensified over the whole SPNA in February 2017. By this mechanism, the advection from the Labrador Sea contributed to create property anomalies in the water column. However, the buoyancy budget showed that this was a minor contribution compared to the buoyancy loss due to the local air-sea flux, even if it was essential to preconditioning the water column for deep convection.

412 We now compare the atmospheric forcing and the preconditioning of the water column in the SECF
413 region with those of the nearby Labrador Sea where deep convection happens almost every year.
414 The atmospheric forcing over the Labrador Sea is ~15 % larger than that over the SECF region: the
415 means (1993 - 2018) of the atmospheric forcing, defined as the time accumulated $B_{surf}^{*} + BF_{ek}$ from 1
416 September to 31 March the year after, are -2.61 ± 0.55 x 10^9 J m^{-2} in the Labrador Sea and -2.18 ±
417 0.54 x 10^9 J m^{-2} in the SECF region. The difference was larger during the period 2016 – 2018 when the
418 atmospheric forcing equaled -3.10 ± 0.19 x 10^9 J m^{-2} in the Labrador Sea and -2.23 ± 0.23 x 10^9 J m^{-2} in
419 the SECF region. In terms of preconditioning, the 2008 – 2014 mean B profile (blue continuous lines
420 in Fig. 7) was lower by ~0.5 x 10^9 J m^{-2} in the Labrador Sea than SECF for the surface to 1,000 m layer
421 and by more than 1 x 10^9 J m^{-2} below 1,200 m. It indicates that the water column was more favorably
422 preconditioned in the Labrador Sea than in the SECF region during 2008 – 2014. Differently, B for
423 W2017 shows slightly lower values from the surface to 1,300 m in the SECF region than in the
424 Labrador Sea (see orange lines in Fig. 7). However, B in the Labrador Sea remains constant down to
425 the depth of the deep halocline between LSW and North Atlantic Deep Water (NADW) at 1,700 m. In
426 the SECF region, the deep halocline remained at ~1,300 m between 2016 and 2018 (see B_s lines in
427 Fig. 7a). Differently, in the Labrador Sea, the deep halocline deepened from 1,200 m for the mean to
428 1,735 m, 1,775 m and 1905 m in W2016, W2017 and W2018, respectively (see dashed lines in Fig.
429 7b). The deep halocline acts as a physical barrier for deep convection in both the SECF region and the
430 Labrador Sea, but because the deep halocline is deeper in the Labrador Sea than in SECF region, the
431 preconditioning is more favorable to a deeper convection in the Labrador Sea than in the SECF
432 region. Summarizing, in winters 2016 - 2018 in the Labrador Sea, both atmospheric forcing and
433 preconditioning of the water column granted the deepest convection depth in the Labrador Sea since
434 the beginning of the Argo period (comparison of our results with those of Yashayaev and Loader,
435 2017). Contrasting, in SECF region, during the same period, the atmospheric forcing was close to
436 climatological values, and the favorable preconditioning of the water column allowed 1,300 m depth
437 convection, what was exceptional for the SECF region.

438 The Labrador Sea, SECF region and Irminger Sea are three distinct deep convection sites (e.g.
439 Yashayaev et al., 2007; Bacon et al., 2003; Pickart et al., 2003; Piron et al., 2017). In this work, we
440 give new insights on the connections between the different sites, showing how lateral advection of
441 fresh LSW formed in the Labrador Sea favored the preconditioning in the SECF region fostering
442 deeper convection.

443 Climate models forecast increasing input of freshwater in the North Atlantic due to ice-melting under
444 present climate change (Bamber et al., 2018), which could reduce, or even shut-down, the deep
445 convection in the North Atlantic (Yang et al., 2016; Brodeau & Koenigk, 2016). We observed a fresh

anomaly in the surface waters in regions close to the eastern coast of Greenland in 2016 that extended to the whole Irminger Sea in 2017 (Fig. S6). However, this surface freshening did not hamper the deep convection in the SECF region possibly because the surface water also cooled. Swingedouw et al., 2013 indicated that the freshwater signal due to Greenland ice sheet melting is mainly accumulating in the Labrador Sea. However, no negative anomaly of S was detected in the surface waters of the Labrador Sea (Fig. S6). It might be explained by the intense deep convection affecting the Labrador Sea since 2014 that could have transferred the surface freshwater anomaly to the ocean interior. This suggests that, in the last years, the interactions between expected climate change anomalies and the natural dynamics of the system combined to favor very deep convection. This however does not foretell the long term response to climate change.

6. CONCLUSIONS

During 2015 – 2018 winter deep convection happened in the SECF region reaching deeper than 1,300 m. The deep convection of W2015 was observed over a larger region and during a longer period of time than the deep convection events of winters 2016, 2017 and 2018. Despite these differences, ~~I~~it is the first time that deep convection, with maximum convection depth larger than 1,300 m, was observed in this region during four consecutive winters.

The atmospheric forcing and preconditioning of the water column was evaluated in terms of buoyancy. We showed that the atmospheric forcing is 10% weaker when evaluated in terms of buoyancy than in terms of heat because of the non-negligible effect of the freshwater flux. The analysis of the preconditioning of the water column in terms of buoyancy to be removed (B) and its thermal and salinity terms (B_θ and B_s) revealed that B_θ dominated the B profile from the surface to 800 m and B_s reduced the B in the 800 – 1000 m layer because of low salinity of LSW. Deeper, B_s increased B due to the deep halocline (LSW-ISOW) that acted as a physical barrier limiting the depth of the convection.

During 2016 – 2018, the air-sea buoyancy losses were close to the climatological values and the very deep convection was possible thanks to the favorable preconditioning of the water column. It was surprising that these events reached convection depths similar to those observed in W2012 and W2015, when the latter were provoked by high air-sea buoyancy loss intensified by the effect of strong wind stress. It was also surprising that the water column remained favorably preconditioned during three consecutive winters without strong atmospheric forcing. In this paper, we studied the reasons why this happened.

The preconditioning for deep convection during 2016 – 2018 was particularly favorable due to the combination of two types of hydrographic anomalies affecting different depth ranges. First, the surface and intermediate waters (down to 800 m) were favorably preconditioned because buoyancy (density) decreased (increased) due to the cooling caused by the atmospheric forcing. Second, buoyancy (density) increased (decreased) in the layer 1,200 – 1,400 m due to the decrease in S caused by the lateral advection of fresher LSW formed in the Labrador Sea. The S anomaly of this layer resulted in a deeper deep halocline. Hence, the cooling of the intermediate water was essential to reach convection depth of 800 – 1,000 m, and the freshening in the layer 1,200 – 1,400 m and the associated deepening of the deep halocline, allowed the very deep convection (> 1,300 m) in W2016 – W2018.

Author contribution: PZ treated and analyzed the data. PZ and HM interpreted the results. PZ, HM and VT discussed the results and wrote the paper.

ACKNOWLEDGEMENT

This paper is a contribution to the EQUIPEX NAOS project funded by the French National Research Agency (ANR) under reference ANR-10-EQPX-40. The Argo data were collected and made freely available by the International Argo Program and the national programs that contribute to it. (http://www.argo.ucsd.edu, http://argo.jcommops.org). The Argo Program is part of the Global Ocean Observing System. The NAO data were downloaded from the UCAR Climate Data Guide website (Schneider et al., 2013): https://climatedataguide.ucar.edu/climate-data/hurrell-north-atlantic-oscillation-nao-index-pc-based. The Ssalto/Duacs altimeter products were produced and distributed by the Copernicus Marine and Environment Monitoring Service (CMEMS) (http://www.marine.copernicus.eu). We thank F. de Jong and two anonymous reviewers, their comments and suggestions have enriched our work.

REFERENCES

Argo Data Management Team: Argo user's manual V3.2. https://doi.org/10.13155/29825, 2017

Argo group: Argo float data and metadata from Global Data Assembly Centre (Argo GDAC), SEANOE, https://doi.org/10.17882/42182 ,2019

Bacon, S.: Circulation and Fluxes in the North Atlantic between Greenland and Ireland. *Journal of Physical Oceanography*, *27*(7), 1420–1435. *https://doi.org/10.1175/1520-0485(1997)027<1420:CAFITN>2.0.CO;2*, 1997.

Code de champ modifié

509 Bacon, S., Gould, W. J. and Jia, Y.: Open-ocean convection in the Irminger Sea, Geophys. Res. Lett.,
510 30(5), 1246, doi:10.1029/2002GL016271, 2003.

511 Bamber, J. L., Tedstone, A. J., King, M. D., Howat, I. M., Enderlin, E. M., van den Broeke, M. R., & Noel,
512 B.: Land Ice Freshwater Budget of the Arctic and North Atlantic Oceans: 1. Data, Methods, and
513 Results, *Journal of Geophysical Research: Oceans*, 1–11,
514 https://doi.org/10.1002/2017JC013605, 2018.

515 Billheimer, S., & Talley, L. D.: Near cessation of Eighteen Degree Water renewal in the western North
516 Atlantic in the warm winter of 2011 – 2012, *118*(November), 6838–6853,
517 https://doi.org/10.1002/2013JC009024, 2013.

518 Brodeau, L., & Koenigk, T.: Extinction of the northern oceanic deep convection in an ensemble of
519 climate model simulations of the 20th and 21st centuries, *Climate Dynamics*, *46*(9–10), 2863–
520 2882. https://doi.org/10.1007/s00382-015-2736-5, 2016.

521 Centurioni and Gould, W. J.: Winter conditions in the Irminger Sea observed with profiling floats,
522 *Journal of Marine Research*, 62, 313–336, 2004.

523 Daniault, N., Mercier, H., Lherminier, P., Sarafanov, A., Falina, A., Zunino, P., Gladyshev, S. : The
524 northern North Atlantic Ocean mean circulation in the early 21st century, *Progress in*
525 *Oceanography*, *146*(June), 142–158, https://doi.org/10.1016/j.pocean.2016.06.007, 2016.

526 de Boyer Montégut, C., Madec, G., Fischer, A. S., Lazar, A., & Iudicone, D.: Mixed layer depth over the
527 global ocean: An examination of profile data and a profile-based climatology, *Journal of*
528 *Geophysical Research C: Oceans*, *109*(12), 1–20, https://doi.org/10.1029/2004JC002378, 2004.

529 de Jong, M.F., Oltmanns, M., Karstensen, J., and de Steur, L.: Deep Convection in the Irminger Sea
530 Observed with a Dense Mooring Array, *31*(February), 50–59,
531 https://doi.org/10.5670/oceanog.2018.109, 2018.

532 de Jong, M. F., & de Steur, L.: Strong winter cooling over the Irminger Sea in winter 2014–2015,
533 exceptional deep convection, and the emergence of anomalously low SST, *Geophysical*
534 *Research Letters*, *43*(13), 7106–7113. https://doi.org/10.1002/2016GL069596, 2016.

535 de Jong, M. F., Van Aken, H. M., Våge, K., & Pickart, R. S.: Convective mixing in the central Irminger
536 Sea: 2002-2010, *Deep-Sea Research Part I: Oceanographic Research Papers*, *63*, 36–51.
537 https://doi.org/10.1016/j.dsr.2012.01.003, 2012.

538 Dee, D. P., Uppala, S. M., Simmons, A. J., Berrisford, P., Poli, P., Kobayashi, S., Vitart, F.: The ERA-

Interim reanalysis: Configuration and performance of the data assimilation system, *Quarterly Journal of the Royal Meteorological Society*, *137*(656), 553–597. https://doi.org/10.1002/qj.828, 2011.

Fröb, F., Olsen, A., Våge, K., Moore, G.W.K., Yashayaev, I., Jeansson, E. & Rajasakaren B.: Irminger Sea deep convection injects oxygen and anthropogenic carbon to the ocean interior. NATURE COMMUNICATIONS | 7:13244 | DOI:10.1038/ncomms13244|www.nature.com/naturecommunications, 2016.

Gaillard, F., Reynaud, T., Thierry, V., Kolodziejczyk, N., & Von Schuckmann, K.: In situ-based reanalysis of the global ocean temperature and salinity with ISAS: Variability of the heat content and steric height. *Journal of Climate*, *29*(4), 1305–1323. https://doi.org/10.1175/JCLI-D-15-0028.1, 2016.

Gill, A. E. (1982), Atmosphere-Ocean Dynamics, vol. 30, Academic, San Diego, CA.

Good, S. A., Martin, M. J., & Rayner, N. A.: EN4: Quality controlled ocean temperature and salinity profiles and monthly objective analyses with uncertainty estimates. *Journal of Geophysical Research: Oceans*, *118*(12), 6704–6716. https://doi.org/10.1002/2013JC009067, 2013.

Josey, S. A., Hirschi, J. J.-M., Sinha, B., Duchez, A., Grist, J. P., Marsh, R.: The Recent Atlantic Cold Anomaly: Causes, Consequences, and Related Phenomena. Annual Review of Marine Science, 10 (1). 475-501.https://doi.org/10.1146/annurev-marine-121916-063102, 2018

Kieke, D., & Yashayaev, I.: Studies of Labrador Sea Water formation and variability in the subpolar North Atlantic in the light of international partnership and collaboration. *Progress in Oceanography*, *132*, 220–232. https://doi.org/10.1016/j.pocean.2014.12.010, 2015a.

Kieke, D., & Yashayaev, I.: Studies of Labrador Sea Water formation and variability in the subpolar North Atlantic in the light of international partnership and collaboration, *Progress in Oceanography*, *132*, 220–232, https://doi.org/10.1016/j.pocean.2014.12.010, 2015b.

Kolodziejczyk, N., Prigent-Mazella A., and Gaillard F. (2017). ISAS-15 temperature and salinity gridded fields**. SEANOE**. http://doi.org/10.17882/52367

Lavender, K. L.,Davis, R. E., & Owens, W. B.: Mid-depth recirculation observed in the interior Labrador and Irminger seas by direct velocity measurements. NATURE |VOL 407 | 7 SEPTEMBER 2000 |www.nature.com, 2000.

Marshall, J., & Schott, F.: Open-Ocean Convection ' Theory , and Models Observations ,. *Reviews of Geophysics*, *37*(98), 1–64. https://doi.org/10.1029/98RG02739, 1999.

Code de champ modifié

Code de champ modifié

Code de champ modifié

570 Ollitrault, M., & Colin de Verdière, A.: The Ocean General Circulation near 1000-m Depth, *Journal of*
571 *Physical Oceanography*, *44*(1), 384–409. https://doi.org/10.1175/JPO-D-13-030.1, 2014.

572 Pickart, R. S., orres, D. J. T and Clarke, R. A.: Hydrography of the Labrador Sea during active
573 convection, J. Phys. Oceanogr., 32, 428–457, 2002.

574 Pickart, R. S., Straneo, F., & Moore, G. W. K.: Is Labrador Sea Water formed in the Irminger basin?
575 *Deep-Sea Research Part I: Oceanographic Research Papers*, *50*(1), 23–52,
576 https://doi.org/10.1016/S0967-0637(02)00134-6, 2003.

577 Piron, A., Thierry, V., Mercier, H., & Caniaux, G.: Argo float observations of basin-scale deep
578 convection in the Irminger sea during winter 2011–2012. *Deep-Sea Research Part I:*
579 *Oceanographic Research Papers*, *109*, 76–90. https://doi.org/10.1016/j.dsr.2015.12.012, 2016.

580 Piron, A., Thierry, V., Mercier, H., & Caniaux, G.: Gyre-scale deep convection in the subpolar North
581 Atlantic Ocean during winter 2014–2015. *Geophysical Research Letters*, *44*(3), 1439–1447.
582 https://doi.org/10.1002/2016GL071895, 2017.

583 Rhein, M, Steinfeldt, R, Kieke, D, Stendardo, I and Yashayaev, I.: Ventilation variability of Labrador
584 Sea Water and its impact on oxygen and anthropogenic carbon: a review, *Philosophical*
585 *Transactions of the Royal Society A: Mathematical, Physical and Engineering Sciences*,
586 375(2102). 20160321. doi:10.1098/rsta.2016.0321, 2017.

587 Schmidt, S., & Send, U.: Origin and Composition of Seasonal Labrador Sea Freshwater, *Journal of*
588 *Physical Oceanography*, *37*(6), 1445–1454. https://doi.org/10.1175/JPO3065.1, 2007.

589

590 Straneo, F, Pickart, R.S., Lavender, K.: Spreading of Labrador sea water: an advective-diffusive study
591 based on Lagrangian data. Deep-Sea Research Part I-Oceanographic Research Papers. 50:701-
592 719, 2003.

593 Swingedouw, D., Rodehacke, C. B., Behrens, E., Menary, M., Olsen, S. M., & Gao, Y.: Decadal
594 fingerprints of freshwater discharge around Greenland in a multi-model ensemble, 695–720.
595 https://doi.org/10.1007/s00382-012-1479-9, 2013.

596 Yang, Q., Dixon, T. H., Myers, P. G., Bonin, J., Chambers, D., & Van Den Broeke, M. R.: Recent
597 increases in Arctic freshwater flux affects Labrador Sea convection and Atlantic overturning
598 circulation, *Nature Communications*, *7*, 1–7. https://doi.org/10.1038/ncomms10525, 2016.

Code de champ modifié

599 Yashayaev, I., Bersch, M., & van Aken, H. M.: Spreading of the Labrador Sea Water to the Irminger
600 and Iceland basins, *Geophysical Research Letters*, *34*(10), 1–8.
601 https://doi.org/10.1029/2006GL028999, 2007.

602 Yashayaev, I., & Clarke, A.: Evolution of North Atlantic Water Masses Inferred From Labrador Sea
603 Salinity Series, *Oceanography*, *21*(1), 30–45. https://doi.org/10.5670/oceanog.2008.65, 2008.

604 Yashayaev, I., & Loder, J. W.: Recurrent replenishment of Labrador Sea Water and associated
605 decadal-scale variability, *Journal Geophysical Research: Oceans*, *121*, 8095–8114,
606 https://doi.org/10.1002/2016JC012046, 2016.

607 Yashayaev, I., & Loder, J. W.: Further intensification of deep convection in the Labrador Sea in 2016.
608 *Geophysical Research Letters*, *44*(3), 1429–1438. https://doi.org/10.1002/2016GL071668, 2017.

609

610 Table 1. Properties of the deep convection SECF and in the Labrador Sea in winters 2015 – 2018. We
611 show: the maximal MLD observed, the aggregate maximum depth of convection ~~Q3~~, the σ_0, S and θ
612 of the winter mixed layer formed during the convection event and n, which is the number of Argo
613 profiles indicating deep convection. The uncertainties given with σ_0, S and θ are the standard
614 deviation of the n values considered to estimate the mean values.

SECF	Maximal MLD (m)	Aggregate max. depth of convection ~~Q3 MLD~~ (m)	σ_0	Salinity	θ	n
W2015	1710	1205	27.733 ± 0.007	34.866± 0.013	3.478 ± 0.130	29
W2016	1575	1471	27.746± 0.002	34.871± 0.003	3.388 ± 0.032	3
W2017	1400	1251	27.745± 0.007	34.868± 0.007	3.364± 0.109	3
W2018	1300	1300	27.748± 0.001	34.859± 0.003	3.263± 0.031	2

LABRADOR SEA	Maximal MLD	Aggregate max. depth of convection (m)~~Q3 MLD~~	σ_0	Salinity	θ	n
W2015	1675	1504	27.733 ± 0.009	34.842 ± 0.010	3.279 ± 0.036	41
W2016	1801	1620	27.743 ± 0.006	34.836 ± 0.010	3.124 ± 0.047	18
W2017	1780	1674	27.752 ± 0.008	34.853 ± 0.009	3.172 ± 0.029	26
W2018	2020	1866	27.756 ± 0.006	34.855 ± 0.010	3.145 ± 0.083	13

615

616

617

618

619

620 **FIGURES**

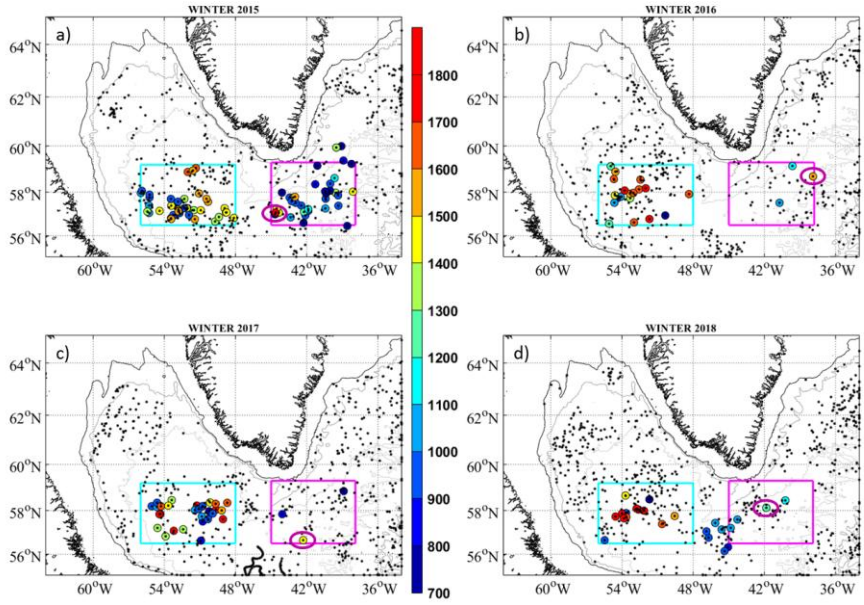

621

622 **Figure 1.** Positions of all Argo float north of 55°N in the Atlantic between 1 January and 30 April a)
623 2015, b) 2016, c) 2017 and d) 2018 (black and colored points). The colored points and color bar
624 indicate the mixed layer depth (MLD) when MLD was deeper than 700 m. The pink circles indicate
625 the position of the maximal MLD observed SECF each winter. The pink and cyan boxes delimit the
626 regions used for estimating the time series of atmospheric forcing and the vertical profiles of
627 buoyancy to be removed in the SECF region and the Labrador Sea, respectively (SECF: 56.5°N –
628 59.3°N and 45.0°W – 38.0°W, Labrador Sea: 56.5°N – 59.2°N and 56°W – 48°W).

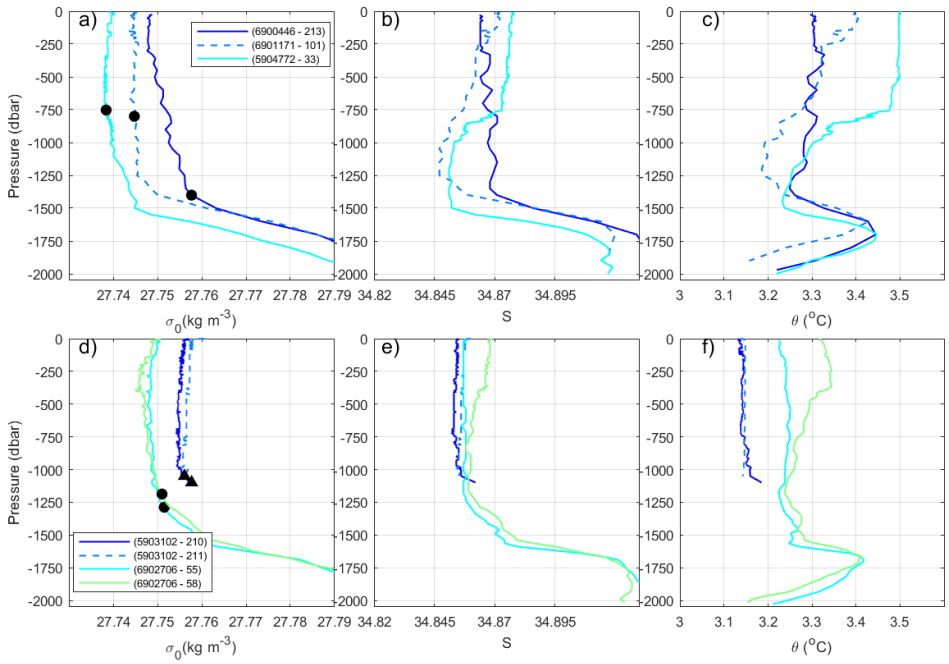

629

630 **Figure 2**. Vertical distribution of σ_0, S and θ of Argo profiles showing MLD deeper than 700 m SECF in
631 Winter 2017 (a, b and c) and in Winter 2018 (d, e, f). The black points indicate the MLD. The triangles
632 in d) are the MLD which coincided with the maximal profiling pressure reached by the float. In the
633 legend, the float and cycle of each profile are indicated.

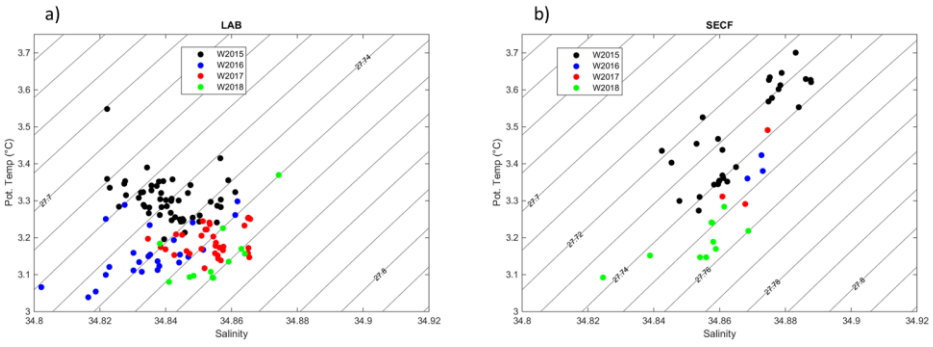

634

635 **Figure 3.** TS diagrams in the mixed layer for profiles with MLD deeper than 700 m during winters
636 2015, 2016, 2017 and 2018 for a) the Labrador Sea and b) SECF. The properties of the mixed layers
637 were estimated as the vertical means between 200 m and the MLD.

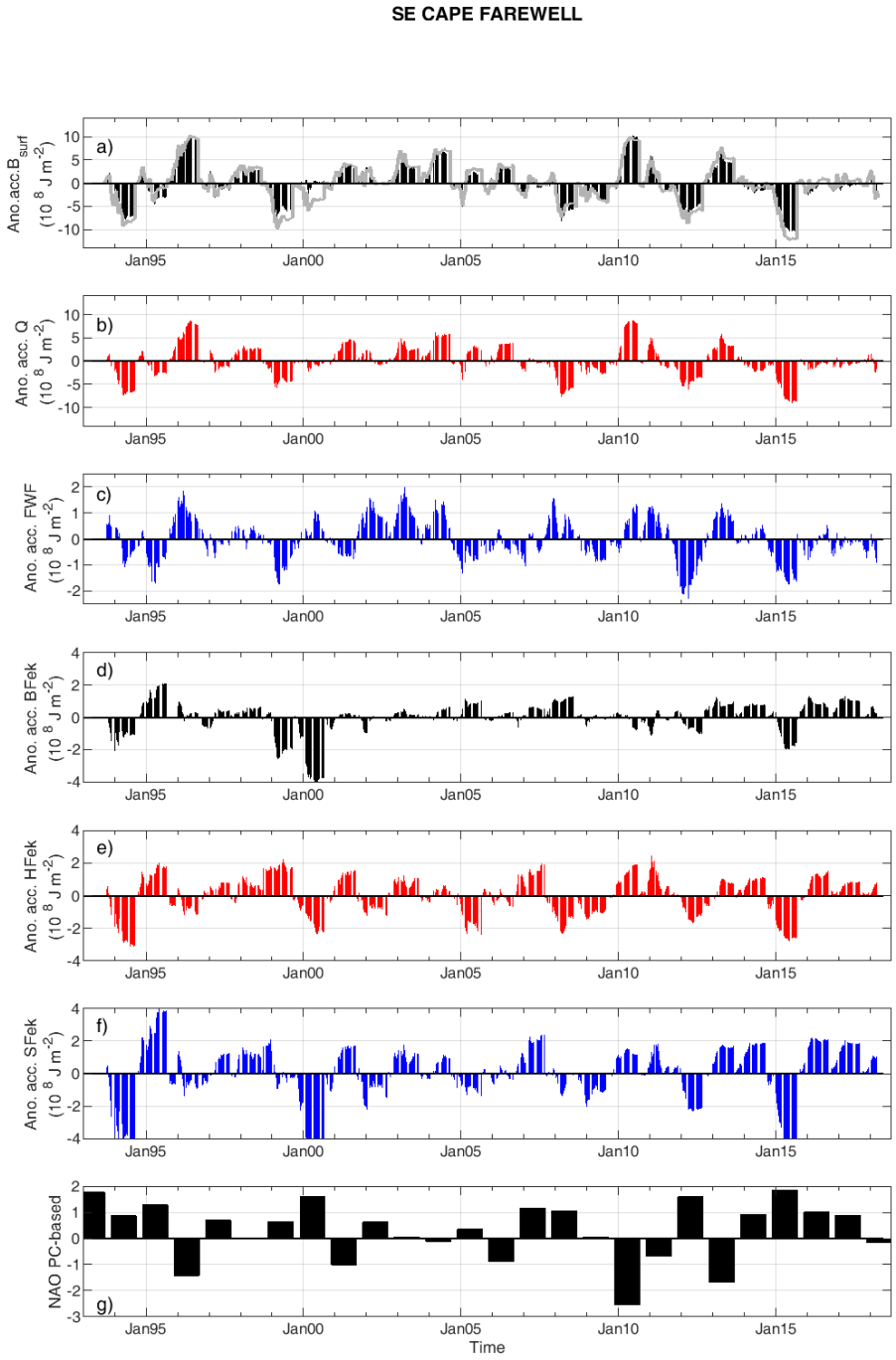

638
639 **Figure 4.** Time series of anomalies of accumulated a) Bsurf*, b) Q, c) FWF* d) BF_{ek} ,e) HF_{ek} and f) SF_{ek},

640 averaged in the SECF region. They are anomalies with respect to 1993 – 2016. The accumulation was
641 from 1 September to 31 August the following year. The winter NAO index (Hurrel et al., 2018) is also
642 represented in g). Gray line in a) is the sum of the anomalies of accumulated B_{surf}* and BF_{ek}. Note that
643 the range of values in the y-axis is not the same in all the plots.

644

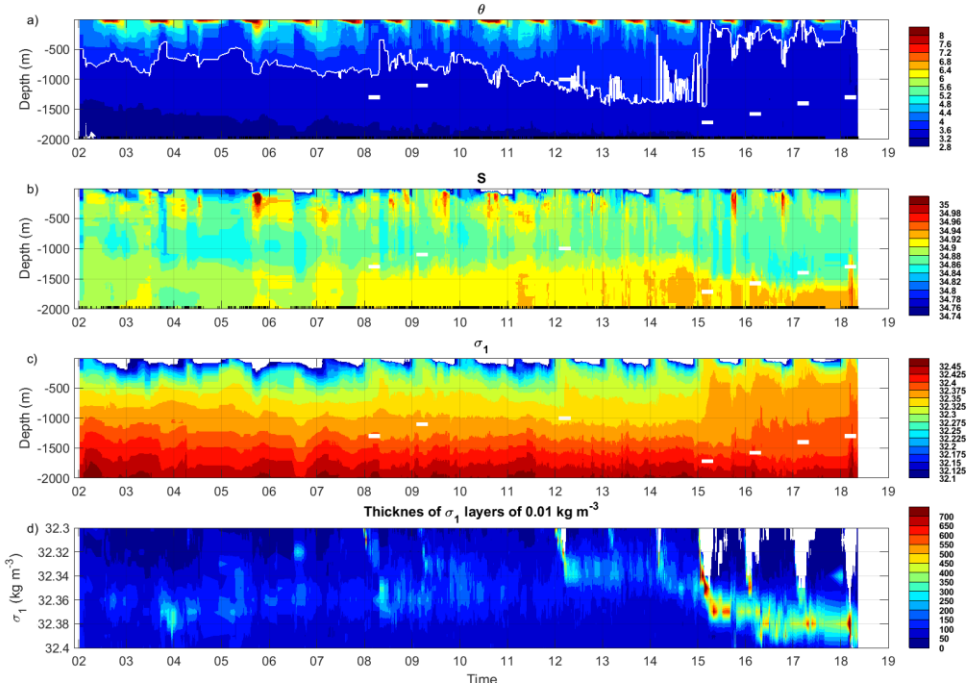

645
646 **Figure 5.** Time-evolutions of vertical profiles measured from Argo floats in the SECF region: a) θ ; b) S;
647 c) σ_1 and d) thickness of 0.01 kg m^{-3} thick σ_1 layers. The white horizontal bars in plots a), b) and c)
648 indicate the maximal convection depth observed in Irminger Sea or SECF when deep convection
649 occurred. The white line in plot a) indicates the depth of the isotherm 3.6 °C. The black vertical ticks
650 on the x-axes of plot b) indicate times of Argo measurements. These figures were created from all
651 Argo profiles reaching deeper than 1000 m in the SECF region (56.5° – 59.3°N, 45°– 38°W, pink box in
652 Fig. 1). The yearly numbers of Argo profiles used in this figure are shown in Fig. S5.

653

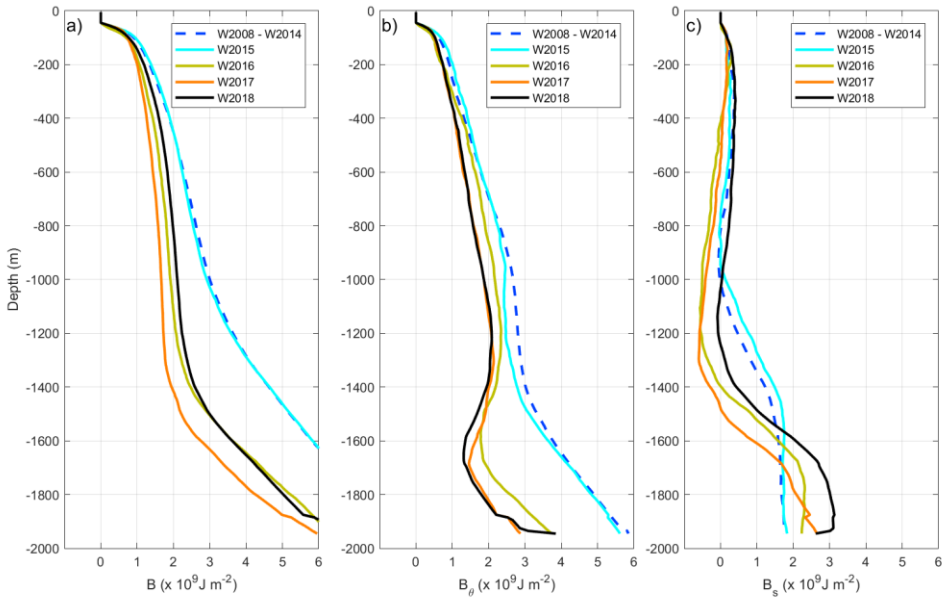

Figure 6. Vertical profile of a) the buoyancy to be removed (B), b) the thermal component (B_θ) and c) the salinity component (B_s). They were calculated from all Argo data measured in the SECF box (see Fig. 1) in September before the winter indicated in the legend. For W2015 and W2018, we considered data from 15/08/2017 to 30/09/2017 because not enough data were available in September. The number of Argo profiles taken into account to estimate the B profiles was more than ten for all the winters.

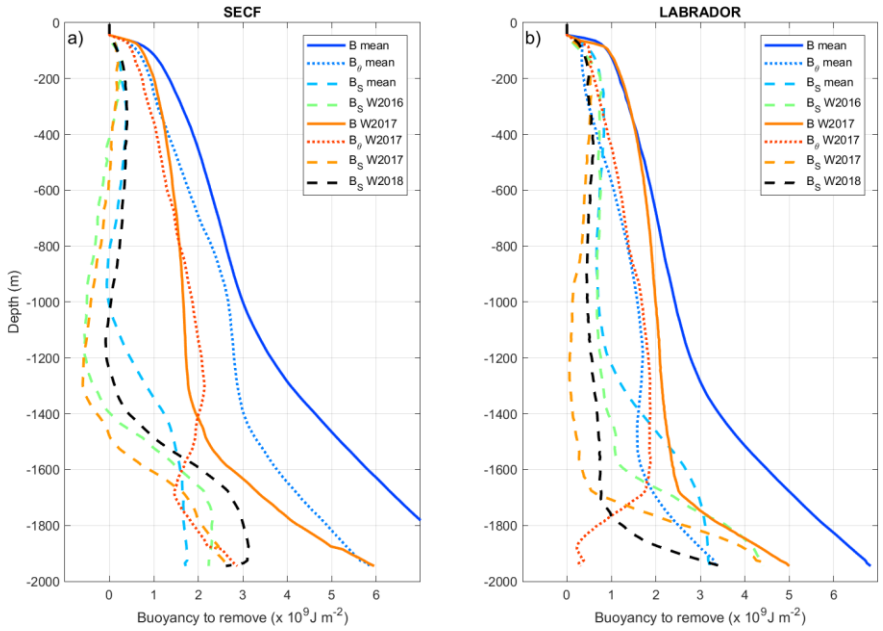

661

662 Figure 7. Decomposition of profiles of buoyancy to be removed (B, continuous lines) in its thermal
663 (B_θ, dotted lines) and salinity (B_s, dashed lines) components in a) the SECF region; b) the Labrador
664 Sea. The B_s components for W2016 and W2018 were added to show the evolution of the depth of
665 the deep halocline.

666

667

668

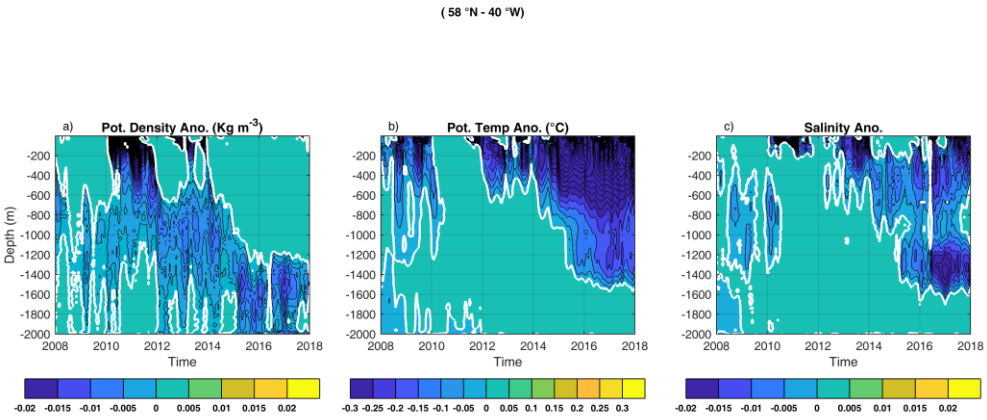

669

670 **Figure 8.** Evolution of vertical profiles of monthly anomalies of a) σ_0, b) θ and c) S, at 58°N, 40°W. The
671 anomalies were estimated from the ISAS database (Gaillard et al., 2016), and were referenced to the
672 monthly mean estimated for 2002 – 2016.

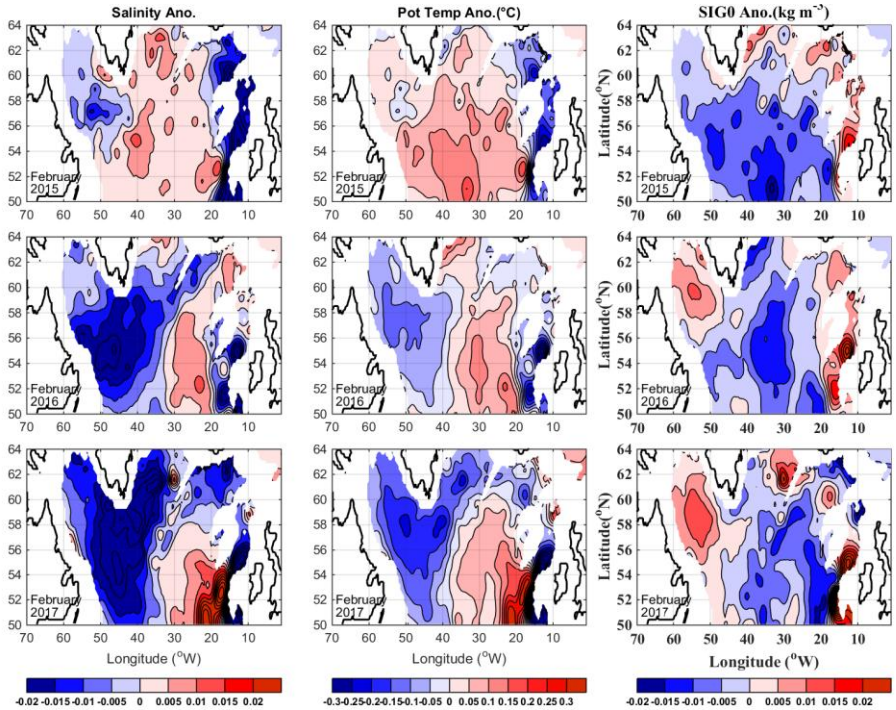

673
674 **Figure 9.** Horizontal distribution of the anomalies of S (left panels), θ (central panels) and σ_0 (right
675 panels) in the layer 1200 – 1400 m in February 2015 (upper panels), February 2016 (central panels)
676 and February 2017 (lower panels). The monthly anomalies were estimated from ISAS database and
677 are referenced to the period 2002 – 2016.

SUPPLEMENTARY MATERIAL

S1. METHODS FOR ESTIMATING THE MIXED LAYER DEPTH

In this paper, mixed layer depth (MLD) was estimated using the threshold method described in section 3.1. Our estimates were compared to those based on the methods of ~~de Jong et al. (2012) and of~~ Pickart et al. (2002), which like ours is adapted to slightly slanted tracer profiles in the mixed layers as those often observed in the central subpolar gyre (Straneo et al. 2002). Pickart et al. (2002) requires a first guess for the mixed layer~~.~~

~~S.1.2. Method of de Jong et al. (2012)~~

~~First, the Argo data were interpolated into 10 m depth steps. Then, we estimated the standard deviations of σ, S and θ from the surface to each depth level. Following de Jong et al., three MLDs were defined as the depths where the standard deviations exceeded 0.05 kg m^{-3}, 0.005 and 0.05°C of σ, S and θ, respectively. The final MLD was the shallowest of the three estimates.~~

~~S.1.2. Method of Pickart et al. (2002)~~

~~We used~~that we have taken equal to the MLD estimate obtained with our threshold method (section 3.1 of this paper) ~~as a first guess for the MLD~~. Then, the mean and standard deviation of the σ, S and θ were estimated from the surface to the initially defined MLD. Finally, the two–standard deviation envelopes overlaid on the original profile were plotted on the σ, S and θ profiles. The mixed layer depth was determined as the location where the profile permanently crossed outside of the two–standard deviation envelope.

S.2. FIGURES IN SUPPLEMENTARY MATERIAL

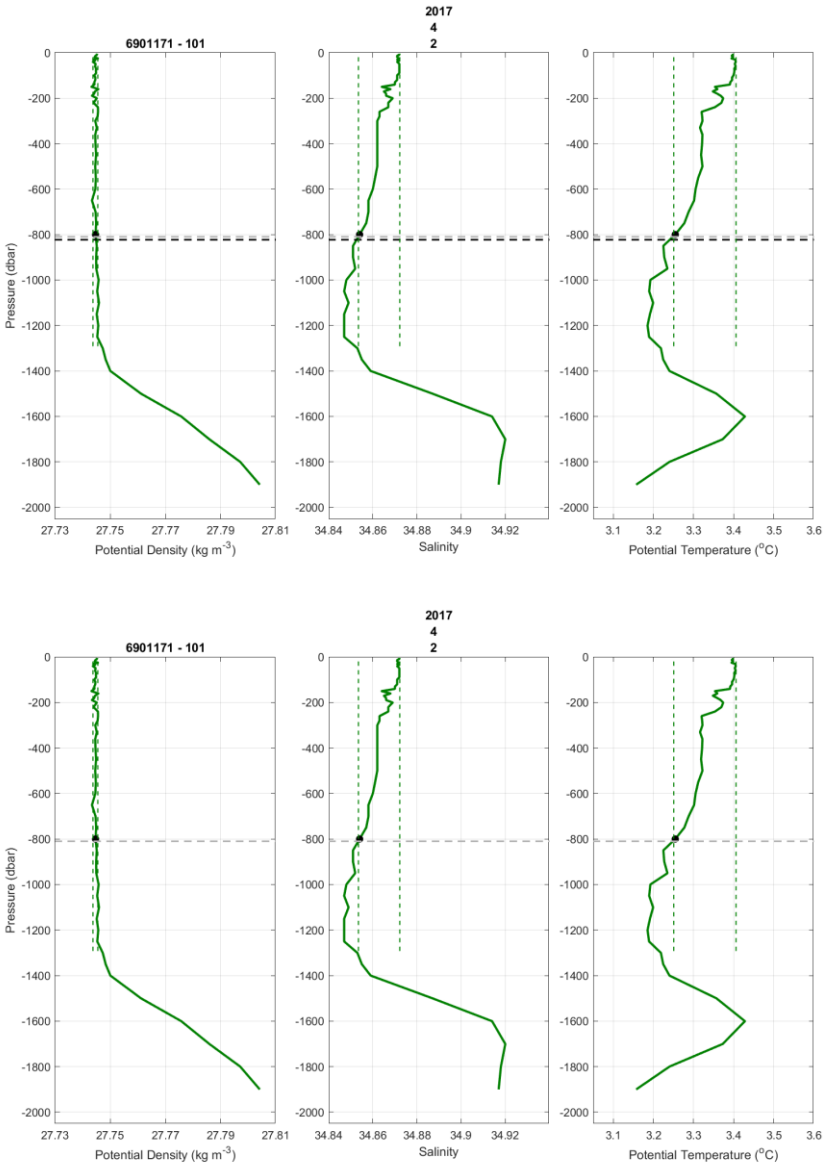

Figure S1. Comparison of MLD estimated for float 6901171 – 101 by our method (black point)~~, by de Jong et al.'s method (horizontal discontinuous black line)~~ and by Pickart et al.'s method (horizontal discontinuous gray line). The continuous colored lines are the vertical profiles of σ, S and θ measured by the Argo float. The dashed colored lines are the two–standard deviation envelope considered in the Pickart et al.'s method.

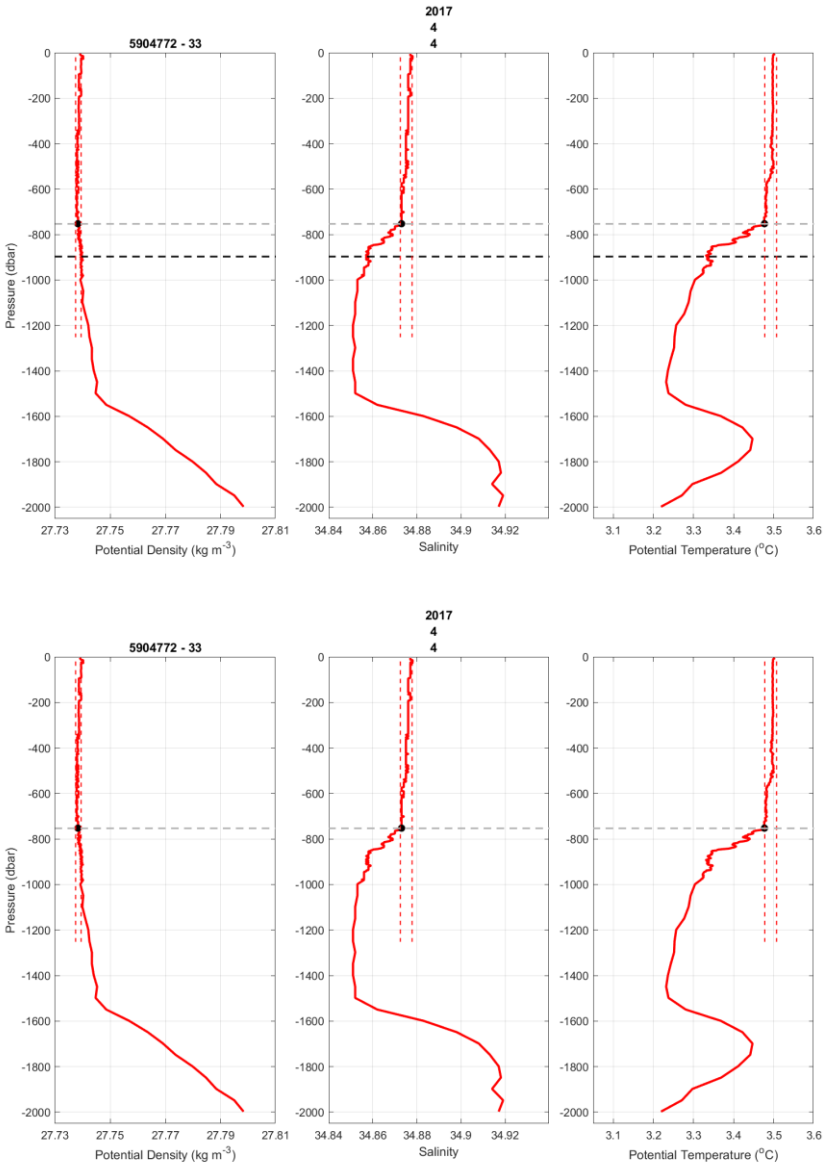

Figure S2. The same as Fig. S1 but for profiles 59004772 – 33.

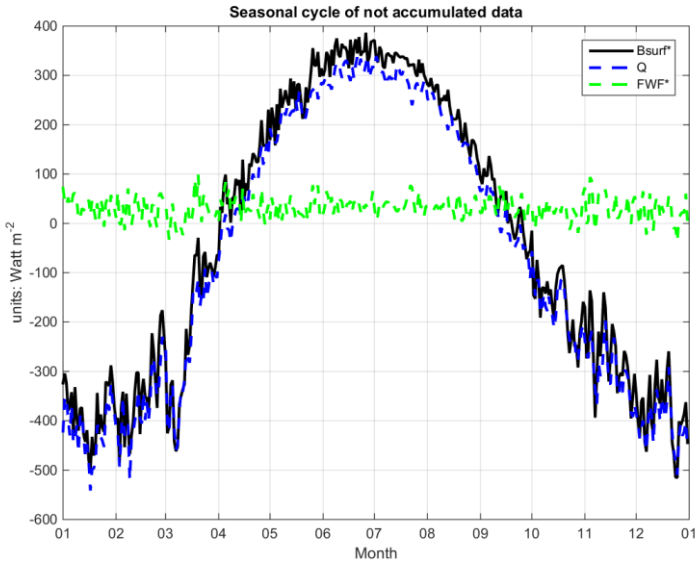

33

34 **Figure S3.** Mean (1993 - 2016) seasonal cycle of air-sea flux of buoyancy (Bsurf*), heat (Q) and
35 freshwater (FWF*) averaged on the SECF region (pink box in Fig. 1). Data origin: ERA-Interim,
36 accumulated every 24h.

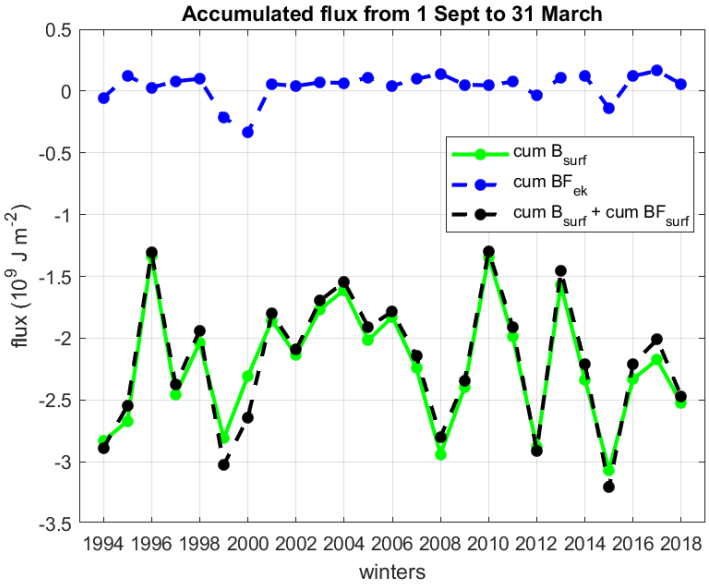

37

38 **Figure S4**. Time series of accumulated (from 1 September to 31 March the year after) buoyancy air-
39 sea flux (B_{surf}) and buoyancy Ekman flux (BF_{ek}) and the sum of both. The year in the x-axes indicates
40 the flux accumulated from 1 September y-1 to March y.

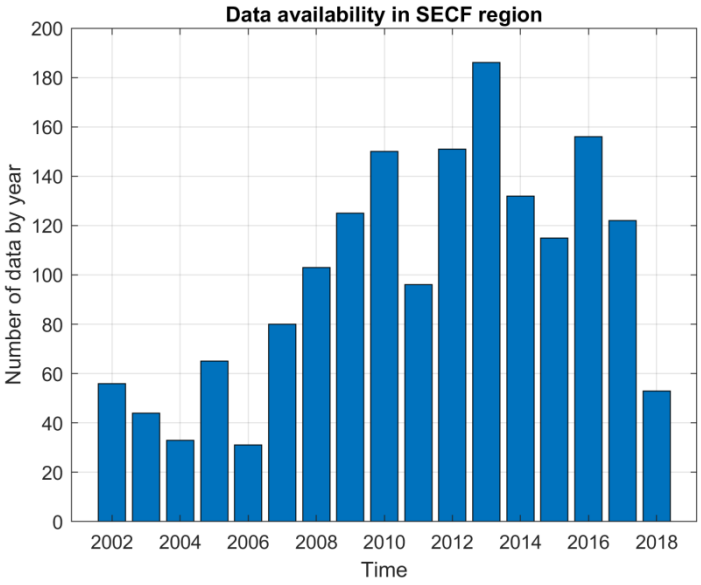

41

42 **Figure S5**. Number of Argo profiles by year used in Figure 5.

43

44

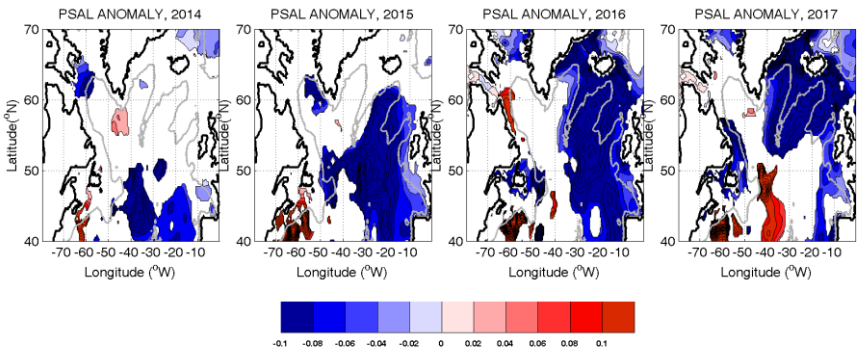

45

46 **Figure S6**. Annual anomalies of salinity in the surface layer (20 – 100 m) estimated from ISAS
47 database. Reference period: 2002 – 2016. We represented only anomalies larger than one
48 standard deviation of the mean.

49

50

References

Pickart, R. S., Torres, D. J. and Clarke, R. A.: Hydrography of the Labrador Sea during active convection, J. Phys. Oceanogr., 32, 428–457, 2002.

Straneo, F., M. Kawase, and R. Pickart: Effects of Wind on Convection in Strongly and Weakly Baroclinic Flows with Application to the Labrador Sea, Journal of Physical Oceanography, V32, *https://doi.org/10.1175/1520-0485-32.9.2603*, 2002.